In situ x-ray diffraction study of the initial dealloying and passivation of $Cu_3Au(111)$ during anodic dissolution

F. U. Renner,[1,2,*] A. Stierle,[2] H. Dosch,[2] D. M. Kolb,[3]
T. L. Lee,[1] and J. Zegenhagen[1]
[1]*European Synchrotron Radiation Facility, 38043 Grenoble Cedex, France*
[2]*Max-Planck-Institut für Metallforschung, 70753 Stuttgart, Germany*
[3]*Abteilung Elektrochemie, Universität Ulm, 89069 Ulm, Germany*
(Received 4 December 2006; revised manuscript received 19 May 2008; published 24 June 2008)

We present an *in situ* x-ray diffraction study of the initial steps of the potential-controlled, selective dissolution of Cu from a $Cu_3Au(111)$ single-crystal surface immersed in 0.1 M H_2SO_4. We followed the structural evolution of an ultrathin Au-rich metallic passivation layer at low overpotentials toward thicker, pure Au islands at elevated overpotentials below the critical potential. The thickness of the ultrathin layer grows from 2 hcp monolayers to several fcc-stacked monolayers. The epitaxial Au-rich layer, which exhibits a reversed stacking with regard to the single-crystal substrate, is passivating the $Cu_3Au(111)$ surface. Complementary *ex situ* atomic force microscopy (AFM) images are also presented and show at elevated overpotentials a surface completely covered with islands of a homogenous size distribution, which agrees well with the findings from the x-ray experiments. The Au islands are found to be weakly hexagonally correlated.

DOI: 10.1103/PhysRevB.77.235433 PACS number(s): 61.05.cf, 68.08.−p, 68.35.Ct

I. INTRODUCTION

Wet electrochemical corrosion of metallic structures is a well-known phenomenon affecting practically all architectures exposed to humidity, from larger-scale constructions down to microelectronic circuits or nanoscale magnetic storage devices. The cost to society of this destructive process is estimated to be around 3% of a national gross domestic product.[1] On one side these electrochemical corrosion processes are detrimental, on the other side the same processes are widely employed in technology. Despite the importance of corrosion processes, today's understanding of the underlying atomic mechanisms and structural processes is still rather incomplete.

An important corrosion process is the selective dissolution of the less noble component of binary alloys. This process, which is commonly called dealloying, has been discussed in the literature since the beginning of corrosion science.[2–4] Alloys such as Cu-Au or Ag-Au have been used for jewelry since centuries, and corrosive surface treatments, named depletion gilding, were employed to change its appearance by enriching the surface with the nobler metal.[5,6] For specific alloy compositions and corrosion conditions, the entire crystal can in fact be dealloyed leaving behind a nanoporous network of the nobler metal.[7–12] In this way, the spongelike metal catalyst "Raney-nickel" had been introduced in chemical industry already in 1926,[13] and further applications were proposed recently, in catalysis,[14] as sensors,[15] nanocrystalline metals,[16] or actuators.[17]

The rather inert Au-based alloys provide, besides their possible applications, an important model system for detailed studies of corrosion and dealloying. The surface structure of binary noble metal alloys was studied within the passivation potential region by transmission electron microscopy (TEM) (Ref. 18) and electrochemical *in situ* scanning tunneling microscopy (STM) (Refs. 19–22). It had been concluded that surface diffusion might be the dominating process in the formation of a passivation layer but no further information about the structure and the chemical composition of the passive layer could be inferred. The formation and coarsening of the porous layer above E_c were addressed by the scanning electron microscopy (SEM) (Ref. 10), small angle neutron scattering (SANS) (Ref. 23), and computer simulations.[24,25]

Recent STM studies,[21,22] on single-crystal Cu-Au surfaces had revealed the occurrence of monoatomic deep vacancy islands with high surface mobility. For $Cu_3Au(111)$, the thickness of the formed metallic passivation layer had been estimated to be a few (1–3) atomic layers based on a proposed surface diffusion model but no direct information on thickness, composition, and structure of these layers could be inferred.

The objective of this x-ray study is to gain detailed information on the atomic structure, morphology, epitaxial relationship, layer thickness, strain, and chemical composition of the formed passivation layers during the initial dealloying process below the critical potential. We have employed surface sensitive x-ray diffraction using highly brilliant synchrotron radiation as an *in situ* tool. It allows reciprocal space studies of the surface-structure evolution of binary alloys during the initial steps of corrosion. A part of the results of this study had recently been published in a short communication.[26] Here we comprehensively describe our results with more important findings and details of the experimental observations.

II. EXPERIMENTAL DETAILS

Cu_3Au crystallizes in the cubic so-called $L1_2$ structure (a_0=375.3 pm). In the ordered alloy, the Au atoms are occupying the corners of the cube and the Cu atoms are occupying the face-centered sites. After mechanical polishing, the $Cu_3Au(111)$ surface was treated with several sputter-annealing cycles under UHV conditions. The surface cleanliness was verified by Auger electron spectroscopy. After

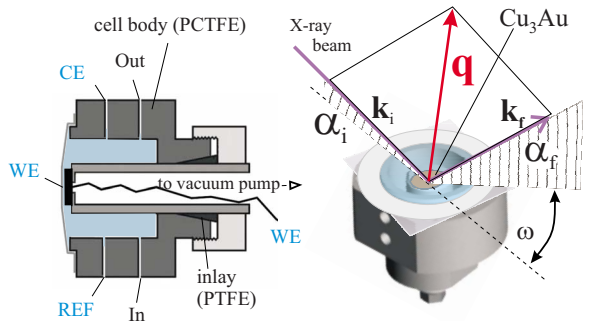

FIG. 1. (Color online) Sketch of the *in situ* x-ray diffraction electrochemical cell. A Mylar foil traps a thin film of electrolyte above the sample (Cu_3Au). In this way, the absorption of the incoming (k_i) and diffracted (k_f) x-ray beam inside the electrolyte is limited.

keeping the sample 30 K below the order-disorder phase-transition temperature (T_c=390 °C) for typically 12 h and cooling down to room temperature, the surface is chemically well ordered, as verified by low-energy electron diffraction. The high quality of the surface $L1_2$ superstructure ordering in UHV was confirmed additionally by synchrotron x-ray diffraction and crystal truncation rod scattering (CTR).[27] After first corrosion experiments using the crystal with well developed $L1_2$ surface order, we allowed the sample to cool down more quickly, which results in a much smaller superstructure domain size (and very broad superstructure peaks). We found no significant differences in the corrosion behavior and the x-ray measurements presented in the following were obtained from crystals with a small superstructure domain size.

Since the corrosion of the sample surface is an irreversible process, the surface preparation procedure was repeated for each experiment. After UHV preparation and characterization, the sample was quickly transferred under ambient conditions into the electrochemical cell. For our *in situ* x-ray diffraction studies we used a thin-film electrochemical cell design with the common three-electrode setup, as shown in Fig. 1. The cell contains connections for the working electrode (sample, WE), the counter (CE) and reference electrodes (REF), and for supply (IN) and outlet of electrolyte (OUT). Cells of this kind have been widely used and described in the literature.[28–34] During the x-ray experiments, the alloy surface was exposed to only a few μm-thin film of electrolytes between the surface and a thin Mylar® foil sealing the electrochemical cell. To allow mass transport at well defined potentials, especially when initiating the dissolution of Cu during the stepwise change of the applied potential, the volume of electrolytes above the sample surface was increased to a thickness of several millimeters by applying a slight overpressure to the solution in the cell. In our *in situ* cell, the CE (a Pt wire), and the Ag/AgCl REF are arranged below the sample surface plane. The sample represents the WE and is held in place inside the electrochemical cell by underpressure with the help of an aspiration hole in the sample holder underneath the WE. This way of mounting assures clean electrochemical conditions and allows an easy exchange of the disklike WE.

For the preparation of the electrolyte solutions we used ultraclean water (18.2 MΩ cm, total organic content TOC <2 ppm) and high-purity acids (suprapure grade, MERCK). All parts in contact with electrolytes had been cleaned in Caro acid and subsequently soaked and rinsed with hot and cold ultraclean water. The sample was immersed into the electrolyte solution inside the cell at a cathodic potential, negative of the expected anodic onset of Cu dissolution (100 mV vs Ag/AgCl). All potentials are given here versus the used Ag/AgCl reference.

The x-ray diffraction experiments were carried out at the insertion device beamline ID32 of the European Synchrotron Radiation Facility (ESRF) in Grenoble, France and at the wiggler beamline BW2 of the Hamburg Synchrotron radiation laboratory HASYLAB in Hamburg, Germany. We used x-ray wavelengths of λ=0.068, 0.11, and also 0.138 nm close to the Cu-K edge at 8.98 keV (in order to exploit anomalous diffraction). The incident angle has been chosen in all cases to lie about 20%–30% above the respective critical angle. The scattering vector $\boldsymbol{q}$ is defined by the difference of the incoming ($\boldsymbol{k}_i$) and diffracted ($\boldsymbol{k}_f$) wave vectors: $\boldsymbol{q}=(\boldsymbol{k}_f-\boldsymbol{k}_i)$ with $|\boldsymbol{k}_i|=|\boldsymbol{k}_f|=2\pi/\lambda$. To describe the reciprocal space of the $L1_2$-Cu_3Au crystal, and the scattering vector $\boldsymbol{q}$, we adopted the commonly used surface unit cell as described in the Appendix with two unit vectors $\mathbf{a_1}$ and $\mathbf{a_2}$ lying in the surface plane and the third unit vector $\mathbf{a_3}$ pointing along the surface normal ($\mathbf{a_1}=\mathbf{a_2}=\sqrt{2}\times\mathbf{a_0}=531$ pm, $\mathbf{a_3}=\sqrt{3}\times a_0=650$ pm, $\alpha=\beta=90°$, and $\gamma=120°$). This leads to a hexagonal reciprocal lattice unit cell of size $\mathbf{a_1^*}=\mathbf{a_2^*}=13.670$ and $\mathbf{a_3^*}=9.666$ nm^{-1}, and $\alpha^*=\beta^*=90°$ and $\gamma^*=60°$ (Fig. 2). Indices (H, K, and L) are given in the following: in reciprocal lattice units (rlu) normalized to the three Cu_3Au reciprocal lattice constants. The cubic unit cell and a {111} plane of Cu_3Au are shown in Fig. 2(e). X-ray diffraction data were recorded using a scintillation counter with an angular resolution of 4 mrad parallel and perpendicular to the surface. The typical counting time was about 1 s for each data point in the scans and reciprocal space maps shown below. Structure factors F were obtained by transversal rocking scans around the surface normal at the respective reciprocal lattice positions, background subtraction and subsequent integration of the obtained peaks (presented here as scattering amplitudes $|A|$, with corrected intensity $I=|A|^2\sim|F|^2$). To extract the scattering amplitudes or structure factors, the standard correction factors were applied.[35] The fit of the structure factor data was performed using the software package ROD.[36]

The atomic force microscopy (AFM) images were recorded with a commercially available Dimension 3100 AFM system (molecular imaging) operated in air. The images were recorded in tapping mode and etched Si tips (MicroMash) with a resonant frequency of typically 315 kHz were employed.

III. RESULTS AND DISCUSSION

A. X-ray diffraction from the Cu_3Au(111) surface in 0.1 M H_2SO_4

In Fig. 3, a (cyclic) voltammogram, i.e., a current-voltage (I-V) diagram, is shown for a pristine single crystalline Cu_3Au(111) electrode. Raising the potential of the electrode beyond its Nernst potential, Cu can go into solution and,

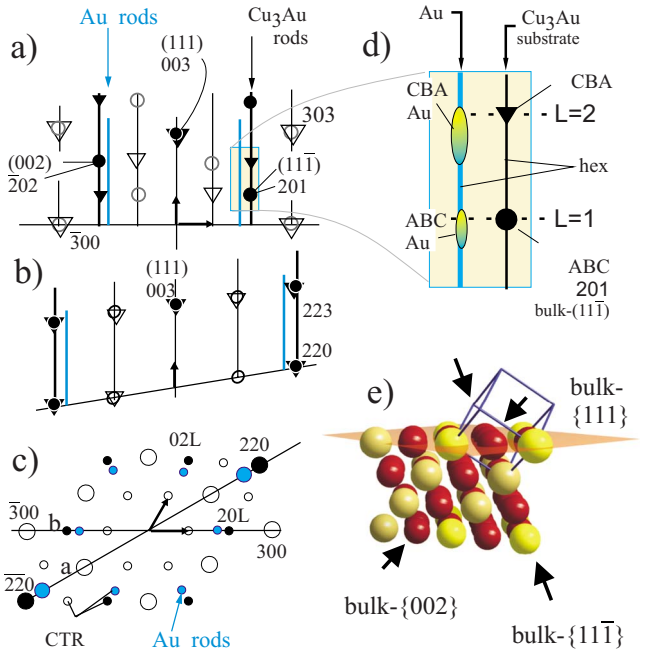

FIG. 2. (Color online) Sketch of the reciprocal space of $Cu_3Au(111)$ and of an Au rich layer [(a)–(d)]. The (H,L), $(H=K,L)$, and (H,K) planes of the reciprocal space are shown, including two twin orientations (triangles and circles), fundamental peaks (filled symbols), and $L1_2$ ordering peaks (hollow symbols). (d) Detail of (a) indicating the positions for the respective stacking in substrate and surface layer. The area corresponds to Fig. 6. (e) Unit cell (real space) of ordered Cu_3Au and the respective {111} plane (bulk values). The {11–1} and {002} planes are indicated.

indeed, an increase in the current is observed in the first cycle. However, the current from the dissolution of the less noble element decreases again, as long as the potential is below the so-called critical potential E_c, at which the less noble element goes massively into solution. The *I-V* curve testifies toward this passivation behavior by exhibiting a strongly diminished dissolution current. It should be noted that in the used acidic electrolyte (pH=1) no bulk Cu oxide

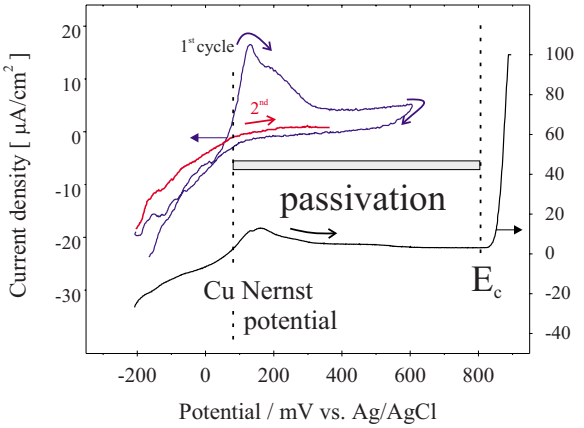

FIG. 3. (Color online) Voltammogram of a pristine $Cu_3Au(111)$ surface in 0.1 M H_2SO_4 solution (5 mV/s) indicating initial Cu dissolution and a passivation phenomenon with very low dissolution currents.

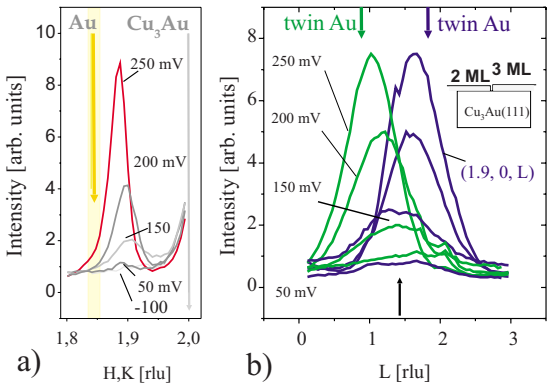

FIG. 4. (Color online) Additional Bragg peaks, indicating the formation of an ultrathin metallic passivation layer, appear with the initial Cu dissolution from $Cu_3Au(111)$ during the first steps of dealloying at low overpotentials. (a) Radial in-plane scans show a growing peak with a relative sharp profile in between the $Cu_3Au(220)$ substrate (gray line) and the Au (220) position at (1.84, 1.84, 0). (b) *L* scans performed along the (1.9, 0, *L*) and (–1.9, 0, *L*) substrate rods. Compare to Fig. 3.

is stable and Cu ions can dissolve directly into the solution.[37] *I-V* curves recorded from pristine alloy surfaces generically show this distinct passivation behavior with an initial dissolution peak at the Nernst potential for the less noble component and a subsequent low current regime below the critical potential E_c. The usual interpretation is that a thin passive layer of the nobler component is formed and protects the alloy from further dissolution. The details of its structure and composition have been left a subject of speculation. In what follows, we will correlate the different potential regimes with our x-ray observations.

1. Behavior at low overpotentials

We first focus on the voltage regime starting from the Cu Nernst potential at 100 mV up to 350 mV ("low overpotential regime"). This regime is far below the critical potential $E_c \approx 800$ mV, which had been determined by potentiodynamic scans.[21] Although the value for the critical potential determined in this way may not be exact,[38,39] our experiments were performed at potentials that were sufficiently lower than the true critical potential. Directly after bringing the sample into contact with the deaerated 0.1 M H_2SO_4 electrolyte (at a potential of –100 mV vs Ag/AgCl), we observed only $Cu_3Au(111)$ substrate reflections as pictured in Fig. 4(a) for the (1, 1) direction. Above +100 mV an additional in-plane Bragg peak can be observed close to the substrate fundamental peak (2, 2, 0.03) and symmetry equivalent peaks. Figure 4(a) shows a sequence of radial in-plane scans for increasing potentials.[40] A new in-plane Bragg reflection appears at (1.9, 1.9, 0), which corresponds to an in-plane lattice constant between the values for Cu_3Au and Au and can be explained by a gold-rich alloy layer.[26] The peaks are centered along the $\langle 1,1,0\rangle$ radial directions of the substrate.[41] From the width of the diffraction peak in the radial (HK) scans, a lateral domain size l of about 12 nm $(l=2\pi/\Delta q)$ can be deduced. As visible in Fig. 4(a), the peak intensities grow with increasing voltage (they also grow

slowly with time), while the peak position shifts slightly toward smaller *HK*, i.e., larger in-plane lattice parameters. Figure 4(b) shows *L*-scans probing (among other parameters) the stacking of the grown layers at different potentials along the two nonequivalent overlayer (1.9, 0, *L*) and (−1.9, 0, *L*) rods, depicted as blue and green curves, respectively. Due to the different in-plane lattice constant of the growing film the respective surface rod of the film is well separated from the CTR of the substrate. Notice the broad maxima in intensity around $L=1.5$ for both surface rods, showing a width along *L* of about $\Delta L=1.5$, associated with a size of $l=2\pi/\Delta q$ corresponding to 2 monolayers (ML). With slightly increasing the overpotentials the width of these diffraction features decreases to about $\Delta L=1$, which corresponds to a thickness of about 3 ML, and the peaks move to different *L* positions for the two rods, i.e., close to $L=2$ for the (1.9, 0, *L*) rod and close to $L=1$ for the (−1.9, 0, *L*) rod.

The (2, 0, *L*) and (−2, 0, *L*) substrate as well as the (1.9, 0, *L*) and (−1.9, 0, *L*) film rods (and their equivalents) are sensitive to the stacking sequence of the close-packed {111} atomic layers along the surface normal. The Cu_3Au substrate shows Bragg peaks at (−2,0,2) and (2,0,1), and we define the associated orientation as "*ABC*" stacking, i.e., the sequence of the substrate. We can thus unambiguously distinguish fcc *ABC* from "*CBA*" stacking sequences, as well as a hexagonal "*ABAB*" sequence. The *CBA* stacking is equivalent to a rotation by 180° (inverted) or 60° relative to the substrate single-crystal orientation.

Thus, we observe at low overpotentials the growth of an ultrathin hexagonal layer which is at first only two monoatomic layers thick. The diffraction peaks are close to $L=1.5$ along the (1.9, 0, *L*) film rods and it show a hexagonal (sixfold) symmetry for rotation around the surface normal. Both are fingerprints of the "*AB*" stacking of the double layer (see Appendix). Increasing the potential further up to 250 mV, the thickness of the passivation film increases to three monolayers and exhibits an fcc stacking, however reversed with respect to the substrate: "CBA…" with characteristic threefold symmetry around the surface normal. We use dashed capitals to indicate the surface layer. The crystallographic orientation corresponds to an epitaxial alignment of $\{111\}_{\text{film}}\|\{111\}_{\text{Cu3Au}}$ and (inverted) $[1,-1,0]_{\text{film}}\|[1,1,0]_{\text{Cu3Au}}$. Similar to our case, x-ray diffraction has been used to determine the stacking sequence of forming xenon layers.[42]

2. Behavior at elevated overpotentials

For the elevated potentials of 400 and 450 mV, we observe a major change in the morphology and composition of the passivation layer, namely the growth of pure relaxed Au islands. We recorded reciprocal space maps, at different potentials, as shown in Fig. 5. Shown are (H,L) plane close to the (2, 0, 1) substrate Bragg peak. Each map was completed in approximately 100 min. From these maps the evolution of the structure and of the surface morphology becomes evident. In Fig. 5(a) we show for comparison a map taken at 270 mV: the broad elongated streak at $H=1.89$ is a characteristic for the ultrathin passivation layer discussed above. At 400 mV an additional Bragg peak becomes visible at slightly

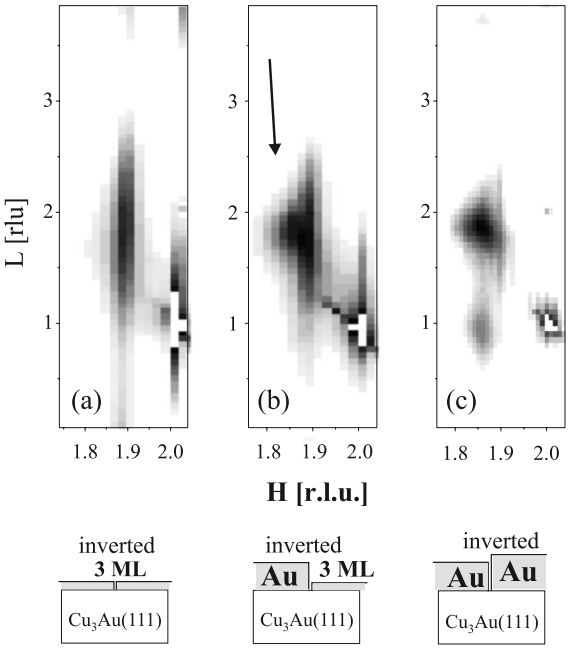

FIG. 5. Top: Reciprocal (H,L) maps close to the (2, 0, 1) Cu_3Au substrate peak [compare to Figs. 3(a) and 3(d)] upon further growth of the metallic passivation layer at elevated potentials. In addition to the substrate peak, which follows the *ABC* stacking sequence, additional intensity maxima are visible: (a) At 270 mV the Bragg reflection characteristic of an ultrathin *CBA*-stacked layer, (b) at 400 mV a peak characteristic of the ultrathin layer and pure Au islands, and (c) at 450 mV intensity coming only from *CBA*-stacked Au islands (with a small contribution of *ABC* stacking). Note the difference in scale of the *L* and *H* axes. Bottom: Schematic representation of the corresponding growth of the passivation layer with increasing potential.

lower *H* value [see arrow in Fig. 5(b)], which is much narrower in *L*. Finally at 450 mV [Fig. 5(c)], the signal from the ultrathin layer has vanished. The map shows an additional peak characteristic of a small fraction of substratelike stacked islands (*ABC*, Bragg peak close to $L=1$).

In the next paragraph we will discuss how the dealloying process depends on the rate at which the potential is increased. When applying a constant overpotential at 300 mV for an extended period of time, the diffraction signal is stable over hours. After a further increase in potential (from 300 to about 400 mV or more), we observe a well separated additional peak at the reciprocal lattice position expected for pure epitaxial Au. The initial peak, characteristic for the ultrathin layer, was vanishing in parallel with time [see Fig. 6(a)].

A more continuous transformation of the ultrathin layer to pure Au islands was observed for the case of a relatively fast increase in potential. The sequence of scans in Fig. 6(b) is recorded during 45 min, i.e., with no waiting period after an initial uninterrupted formation of the ultrathin layer. As before, we observe a first peak close to (1.9, 1.9, 0), which grows in intensity with increasing the potential. At 400 mV the Bragg peak starts to shift as a whole, continuously toward the pure Au position. Instead of coexistence during the transition, the complete initial ultrathin layer is gradually transformed into thicker and more Au-rich islands.

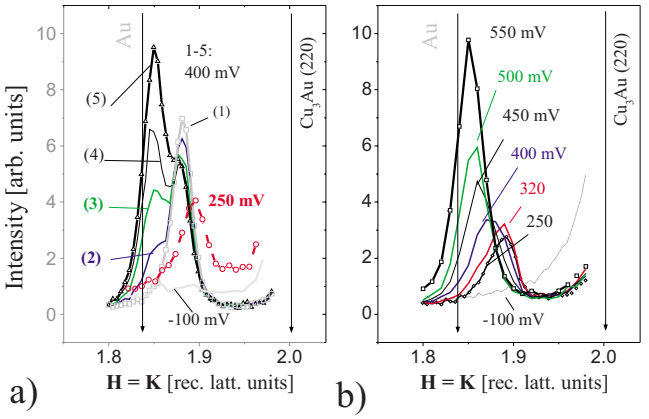

FIG. 6. (Color online) Radial *HK* scans showing further growth of the metallic passivation layer at elevated potentials. (a) In-plane radial scans for a fast increase in applied potential. The passivation layer peak decreases as a function of time and a Bragg peak grows close to the position of pure Au. (b) In-plane radial scans for a slow increase in applied potential. The in-plane peak shifts continuously toward the position expected for epitaxial Au islands.

The detailed growth behavior of the passive overlayer is thus different for a slow and a fast increase in potential. A reason could be that the number of structural defects, which might be present after nucleation of the thin alloy layer, will decrease when the potential is kept constant for some time by a surface mediated healing process.

3. Analysis of the surface layer rod for a substrate potential of 270 mV

In Fig. 5(a) we have shown the elongated reciprocal space intensity distribution which is characteristic for an ultrathin layer. The intensity along this surface rod is originating from the freshly formed metallic passivation layer alone. By a comparison of the measured to the calculated intensities a structural model of the passivation layer can be derived.

The surface layer was prepared by slowly increasing the potential from −100 to 270 mV after immersion of the sample into 0.1 M H_2SO_4 electrolyte. At this potential the structure was stable within the typical data collection timescale of several hours. The intensities of the surface layer rod (corrected intensity $I=|A|^2\sim|F|^2$) were recorded at a fixed potential of 270 mV. Each rod [(1.9, 0, *L*), (−1.9, 1,9, *L*)…] represents the average of several equivalent rods (and the resulting error bars). Figure 7 shows the obtained scattering amplitude $|A|$ for three nonequivalent rods and a fit to the data (gray line) obtained from a simple structural model. This model (Fig. 8) consists of Au layers and is built up by a first layer with 91% occupancy, a complete second layer followed by one-half occupied third layer, and an additional fourth (top) layer with low occupation (9%). These layers are forming an fcc-like structure with a reversed stacking sequence (*CBA*) as compared to the substrate. Note here that a lower occupancy may also be explained by a partial Cu content in the layers. No domains of substratelike (*ABC*) stacking sequence were included in the model. The in-plane lattice parameter has been deduced from the in-plane scans, while the *z* distances of the respective layers and their occupancy

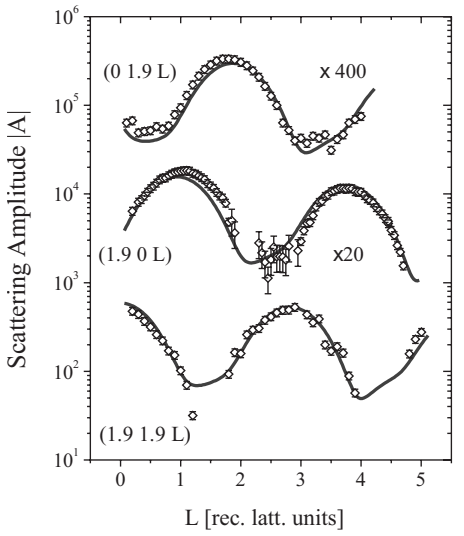

FIG. 7. Measured and corrected scattering amplitude and the result of model calculations for the best fit to the data for three different surface rods. The structure model is shown in Fig. 8. For clarity, two rods are shifted by multiplication with the indicated factors.

have been varied in the fitting procedure. The fitting model presented here resulted in a χ^2 value of four. In plane as well as perpendicular to the surface the lattice parameters and layer distances are larger than for Cu_3Au but smaller than for pure Au (d_{perp}=235 pm). In our fitting procedure we allowed for a free absolute scale factor as the absolute intensity of the incoming beam was not measured, and therefore the calculation did not allow us to clearly distinguish between Cu (29 electrons) and Au (79 electrons) contributions. However, our previously reported anomalous scattering[26] experiment had revealed a Cu content of about 40% for a surface layer that was prepared at the same potential. The presented fit shows some deviation to the data at *L* values around *L* =1.5 rlu. It is worth noting that an introduction of about 10% of Au atoms occupying hexagonally coordinated positions leads to a slightly lower χ^2. Additionally allowing the Debye–Waller factor to be larger than the literature value leads to better fitting results (χ^2 of 2.52 for the latter case). A

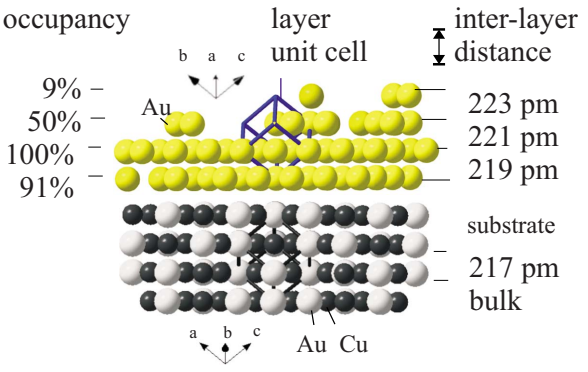

FIG. 8. (Color online) Model for the fit to the CTR data of Fig. 7. The substrate (Cu as black and Au as gray balls) and the pure strained Au layer assumed in the fit model are shown. The parameters of the fit model are indicated.

large Debye–Waller factor can also result from static disorder at the interface, which may be caused by the incommensurate nature of the Au-rich overlayer on the substrate (5% in-plane lattice mismatch results in a commensuration cell of 20×20 surface units). However, due to the relatively small data set, it is not justified to use a large number of free parameters in the fitting procedure. Our simple model (Fig. 8) consisting of about 3 ML of distorted Au reproduces the main features of the data fairly well.

4. Structure of the $Cu_3Au(111)$ *surface/interface*

Measurements of integrated intensities along CTRs can be used to deduce the detailed structure of the surface or interfaces of crystals either by comparison to model calculations[43] or using state-of-the-art direct methods and refinement.[44] The magnitude of the intensity along the CTRs in between the Bragg reflections is determined by the detailed surface structure and the surface quality, e.g., the surface roughness. The pristine $Cu_3Au(111)$ surface after preparation in UHV was described in a previous publication[27] as exhibiting an ordered $L1_2$ structure well up to the topmost layer with large terrace sizes.

The ultrathin passive layer adopts a different lattice constant in the surface plane (see previous section). The scattering of this layer is well separated from the substrate signal. With the surface layer present, the substrate CTR intensity is thus sensitive to the structure of the interface between substrate and surface layer. The $Cu_3Au(111)$ CTR data displays a clear decrease in intensity as soon as the sample is exposed to air at ambient pressure (data not shown here). Immersion in an electrolyte with an application of low and moderate overpotentials (here up to 450 mV) leads only to a little further drop in intensity along the CTR. We believe that the overall decrease in CTR intensity originates in a large part from an increase in roughness after exposure to air. This may be produced by some oxidation of the surface Cu and the subsequent dissolution of the oxides in the acidic electrolyte. Interestingly enough, the roughness increases hardly with the dissolution of Cu and the formation of the new surface layer. A reasonably flat interface is therefore retained during the initial Cu dissolution below 450 mV.

IV. *EX SITU* AFM IMAGES

In addition to the *in situ* x-ray work, *ex situ* AFM experiments have been performed [Figs. 9(a)–9(d)]. The results presented here were obtained from samples prepared using a classical electrochemical cell, without x-ray exposure. Samples that were imaged after x-ray experiments revealed qualitatively similar patterns depending chiefly only on the applied potentials.

In Fig. 9(a), an AFM image of a clean $Cu_3Au(111)$ surface is shown, obtained in ambient air after preparation of the $Cu_3Au(111)$ surface in UHV. The image clearly shows single atomic steps and flat terraces. The apparent roughness on the terraces can be explained by adsorbed water or oxygen molecules during the measurement in ambient air. The corresponding height–height correlation function (HHCF) is shown in Fig. 9(e). After contact of such a clean $Cu_3Au(111)$ surface with deaerated 0.1 M H_2SO_4 solution at 250 mV for 1 h, the images look similar to the initial surface with a moderately increased roughness [Fig. 9(b)]. However, the HHCF is now significantly different, showing distinct side peaks on each side of the central maximum. An image with a sample kept in contact with electrolyte at 400 mV for 3 min shows very clearly a surface that is densely packed with islands of homogeneous size [Fig. 9(c)]. The two-dimensional (2D) HHCF plots of some of the images reveal an average hexagonal arrangement of the islands [inset of Fig. 9(c)].

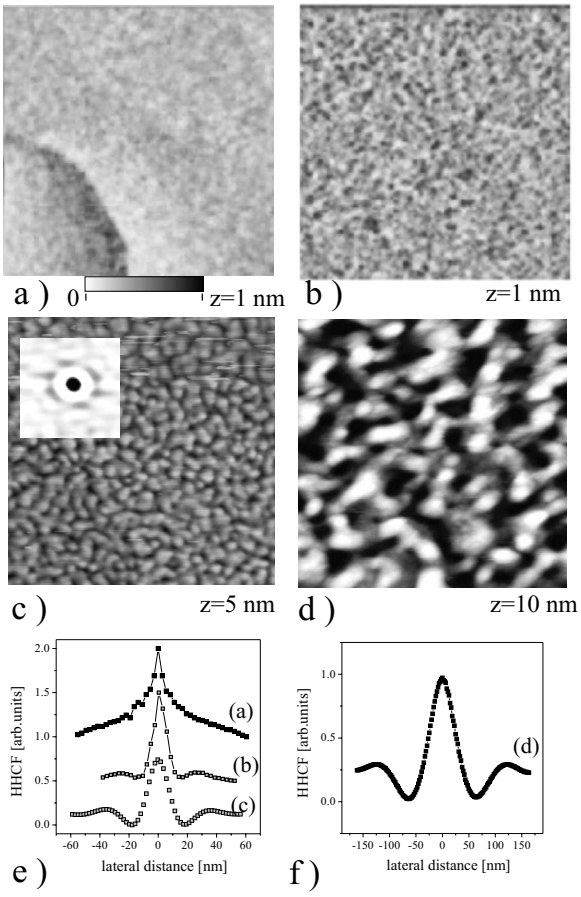

FIG. 9. *Ex situ* AFM images (500×500 nm^2) and HHCF curves. (a) Clean $Cu_3Au(111)$ surface in air after UHV preparation. (b) $Cu_3Au(111)$ surface after 1 h of contact with 0.1 M H_2SO_4 at 250 mV. (c) $Cu_3Au(111)$ surface after 1 h of contact with 0.1 M H_2SO_4 at 400 mV. The inset shows a 2D HHCF of a part of the image (not to scale). (d) Image of a part of the $Cu_3Au(111)$ surface after 10 h of *in situ* x-ray measurements in 0.1 M H_2SO_4 at 400 mV. At other parts of the surface the sample looked similar to (c). (e) HHCF obtained from AFM images [(a)-(c)]. (f) HHCF obtained from AFM image (d).

A different surface morphology develops after long (>10 hours) exposure at 400 mV [Fig. 9(d)]. In addition to the dense islands usually observed at 400 mV, some regions with a porous surface are observed, which also show a hexagonal 2D HHCF pattern but with a larger distance between the islands/ligaments [Fig. 9(f)]. Hexagonally closed-packed islands have been observed in a growth study of Au on amorphous substrates, although the Au islands in this study were

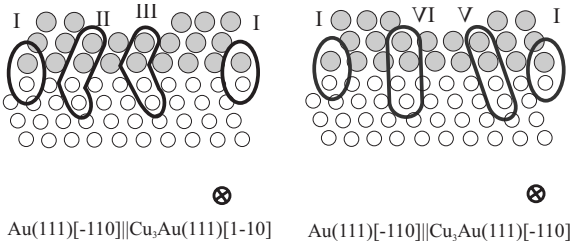

FIG. 10. Sketch of a heterophase-interface formed by an ultrathin Au rich layer (with a different in-plane lattice parameter) on $Cu_3Au(111)$. The difference in interface energy of a surface layer (a) with substrate stacking sequence and (b) with an inverted stacking is created by a different distribution of local stacking arrangements at the interface. The local regions of a simple hard-sphere model representing the respective interface include on-top (I), hcp-fcc (II), fcc-hcp (III), hcp-hcp (IV), and fcc-fcc (V) coordination.

not as flat as in our case but rather moundlike.[45] The weakly hexagonal superstructure of the island distribution and the change of the morphology with time is an indication of diffusive exchange between the islands. It could be reminiscent from an initial spinodal decomposition of the first substrate layer at the beginning of the process, as some similarities in length scale are apparent in comparison to Au surface layers produced by spinodal decomposition in electrochemical environment.[46] Moreover, a spinodal decomposition is in line with a computer simulation of the initial dealloying of Ag-Au.[24,25]

V. FURTHER ANALYSIS AND DISCUSSION

The *in situ* x-ray diffraction experiments allowed us to follow the structural evolution of the (111) surface of the binary alloy Cu_3Au. At low overpotentials we first observed an initial ultrathin Au-rich layer. As obvious from the separated in-plane diffraction peaks, the in-plane lattice parameters of the film and the substrate are different. Due to its 5% larger lattice parameter, the first close-packed Au-rich atomic layer will occupy continuously changing sites with respect to the $Cu_3Au(111)$ surface. In Fig. 10 we show the sketch of heterophase interfaces created by an inverted and a substrate-like stacking in a surface layer with a larger in-plane lattice constant. At such an incoherent interface differently coordinated, energetically favorable and unfavorable regions are (locally) created, alternating along the interface. These include fcc-coordinated sites (ABC-A'), hcp (ABC-B'), and as well as on-top sites (ABC-C'), where positions of atoms in the first layer of the film are denoted by dashed capitals. The second layer of the new Au-rich surface structure will then determine the orientation (stacking sequence) of the forming fcc-like passive layer, and it will thereby create specific local coordination regions (Fig. 10 I–VI). The third layer will define whether the passive film grows with hcp or fcc structure. We observe that it grows in the fcc structure and without any doubt solely the new reversed stacking sequence $C'B'A'$ is formed in the surface layer (or $B'A'C'$ or $A'C'B'$, which are equivalent except for the position of the first atom). There are reports in the literature of an fcc-hcp slide of some of the atoms of the topmost substrate layer, e.g., at an Au/Ni(111) interface, in order to avoid the unfavorable on-top arrangement[47,48] (ABC-$C'B'$ instead of ABC-$C'B'$). We do not have sufficient information to clarify whether this is relevant for our case. The local coordination regions across the interface consist of laterally separated mixed fcc-hcp (II) and hcp-fcc (III) regions in the case of the observed inverted ultrathin film. We do not observe aligned stacking ($A'B'C'$), which would exhibit purely hcp (IV) and purely fcc (V) interface regions. The reversed $C'B'A'$ stacking with its mixed regions is obviously energetically favored for the ultrathin passive layer.

Preferred stacking reversal was observed in ultrathin, incommensurate Au films on Ni(111) and a few other systems in UHV,[48–50] and entirely reversed, incommensurate oxide layers have been evidenced on Ni(111)[51] and on Cu(111)[52] when grown electrochemically in solution. In spite of the growing number of experimental reports of such inverted incoherent fcc(111)/fcc(111) interfaces, there are no theoretical calculations so far to shed some light on the microscopic energy landscapes of such interfaces. This is possibly due to the somewhat larger unit cells necessary to describe the structures involved. For the simpler case of coherent epitaxial $NiSi_2$ on Si(111), e.g., both types of stacking, called A-type and B-type epitaxy, can be realized by proper growth conditions.[53] This interface had been addressed also by first-principles calculations.[54] The formation of the new reversed surface structure requires diffusion within the topmost layers, but we cannot decide whether surface diffusion [as was suggested based on recent scanning tunnel microscope (STM) studies[19,21]] or a bulk diffusion process[55] is at work. However, in a more recent experiment with a chloride additive to the electrolyte, we observed a negative shift in the potential for the transition of the ultrathin layer to the Au islands, which indicates a dominating contribution of surface diffusion to the formation process of the passive layer.[56] Also the above described hexagonal correlation in the AFM images points to a diffusive exchange of atoms between the formed islands, most probably via the surface or the electrolyte.

The peak position in reciprocal space contains information on the crystallography and indirectly on the chemical composition and internal strain (revealed by the size of the three-dimensional unit cell). In the following we present further analysis and discussion of the peak position of the x-ray diffraction data recorded during the formation of the passive Au rich layer. Figure 11 shows a plot of the in-plane versus the out-of-plane lattice constants that were deduced from the peak positions in the respective HK and L scans. The $\{2,2,0\}_{\text{bulk}}$ and $\{1,1,1\}_{\text{bulk}}$ planes of Cu_3Au have a distance of 133 and 217 pm, respectively. These lattice plane distances for the Cu_3Au substrate are marked by the filled circle in Fig. 11 and are placed on the line, which connects the corresponding spacing of pure Cu and pure Au. They follow Vegard's Law, which is approximately valid for the system Cu-Au. Figure 11 shows, in addition, the lattice constants of the ultrathin fcc Au-rich overlayer and the pure Au islands. For the ultrathin layer only values that were deduced from at least two nonequivalent L scans have been included. This procedure was necessary because the contribution to the scattering originating from regions with the thinner, 2-ML-thick

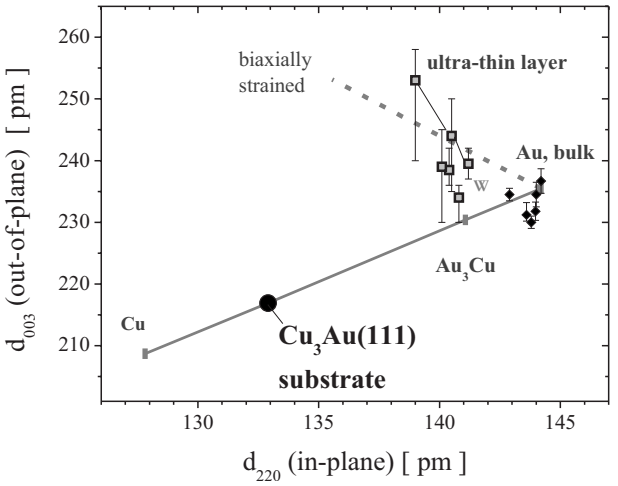

FIG. 11. Plot of the measured in-plane lattice parameters versus the perpendicular interlayer distance (out-of-plane). This plot aids to rationalize possibly present strain and effects of different compositions in the formed passivation layers. The ultrathin layers lie in the region between strained pure Au (111) layers (dashed line) and relaxed Cu-Au alloys (continuous line). The thicker Au islands possess lattice parameters very close to relaxed bulk Au. The equilibrium structure of 3 ML (0.7 nm) of a freestanding Au layer as calculated by Wolf (Ref. 55) was marked by (*w*).

layer to the diffraction signal causes a systematic shift of the weight of the peak. [compare to Fig. 3(d)]. The values determined from the peak position of only one rod are thus systematically too small or too large and this fact is responsible for the large error bars. (This shift is related to the well-known peak shifts observed for a high stacking fault density in fcc bulk samples).

The thicker islands that were formed at elevated overpotentials exhibit lattice constants close to pure bulk Au. Less clear is the situation for the initial ultrathin layers. The in-plane and out-of-plane lattice parameters spread in the triangle between the line for Vegard's Law and the line expected for biaxially strained pure Au(111) films (dashed line, plotted here using bulk elastic constants). The detailed microscopic "path" of the lattice of the initial passivation layer depends on the way the experiment is performed, i.e., the applied potential-time curve. However, the lattice parameters of the freshly formed ultrathin passive film structure stays within the range of the parameters for a relaxed Cu-Au alloy film, which contains not more than 40% Cu and a highly strained ultrathin pure Au film (we had reported in a previous publication[26] that the ultrathin passive layer contains about 40% Cu). Interesting in this context is the fact that the Au(111) surface is well known to reconstruct by the formation of a compacted topmost surface layer (4.2% in the ⟨100⟩ directions[32]). Similar, calculations for freestanding Au films[57] also resulted in a surface-stress induced in-plane contraction of ultrathin films. Furthermore, an ultrathin Au film on Ni(111) with increased density compared to bulk Au was recently observed by medium energy ion scattering.[48] Therefore we propose that the detailed value and time over which the potential is applied can influence the actual concentration of residual Cu in the film during the fast initial layer formation. Additional strain might build up after the lattice is initially formed and Cu atoms are released and replaced by Au. After formation of the initial film, strain can only be released by forming dislocations. In the potential region in which we observe the structural transition of the ultrathin layer to the Au islands, additional electrochemical processes might well play a role. For instance, on Au(111) single-crystal surfaces in H_2SO_4 electrolyte adsorption of sulfide ions takes place at about 400 mV (Ref. 58), while in Cu-ion containing solutions also underpotential Cu deposition (UPD) is observed.[59] Understanding the exact microscopic mechanisms involved in the observed structural transition will require further investigation.

VI. CONCLUSIONS

We presented an *in situ* x-ray diffraction investigation of the selective dissolution of Cu from $Cu_3Au(111)$ in 0.1 M H_2SO_4 far below E_c, complemented by an *ex situ* AFM study. Note that such crystallographic details on freshly forming, only monolayers thick, surface layers are difficult to obtain with other techniques. Here, *in situ* x-ray diffraction provides unique knowledge, complementary, e.g., to the widely used scanning probe techniques. Our study in the potential range up to 450 mV revealed two potential regimes with two different structures of the metallic passivation layer. We observed ultrathin, about 3-ML thick, strained Au-rich layers at low overpotentials (100–400 mV) and 10–20-ML-thick (2–5 nm) pure, relaxed Au islands at elevated overpotentials (400–450 mV). The formed fcc-like passivation layers exhibit an inverted stacking sequence of the {111} layers compared to the substrate. The morphology of the island-covered surface was imaged by *ex situ* AFM and fits well with the x-ray results. The islands show a weak hexagonal height–height correlation which points to the presence of an interisland diffusion path.

ACKNOWLEDGMENTS

Financial support by the German BMBF under Contract No. 05KS1GUC3 is gratefully acknowledged. We thank B. Krause, A. Reicho, S. Warren, B. C. C. Cowie, S. Thiess, O. Bunk, and W. Drube for their help with the synchrotron measurements at ESRF and HASYLAB, and F. D'Anca and R. Felici for collaboration in developing the *in situ* cell and installing the electrochemistry laboratory at INFM-OGG/ESRF.

APPENDIX: RECIPROCAL SPACE OF CLOSE-PACKED CRYSTALS

To facilitate the understanding of the results presented, we shortly describe the reciprocal space of close-packed single-element crystals. Hexagonally arranged close-packed atomic planes (denoted *A*, *B*, or *C* in the following) can be densely stacked by subsequently filling tetrahedrally coordinated sites. Such a stacking mostly results either in the face-centered-cubic (fcc) *ABCA*… stacking, or in a hexagonally close-packed (hcp) *ABA*… sequence, depending on whether the atoms in every second or every third layer are exactly on

top of the atoms in the first layer. Starting with an atomic plane A, the fcc type can exist in a second variant with an $ACBA\ldots$ stacking (and thus called inversed, or twinned structure), which is identical to the former but rotated by 60° (or 180°) around the normal of the close-packed atomic plane. All such crystals can be described in similar hexagonal unit cells with a rhombohedral base with $\alpha=\beta=90°$ and $\gamma=120°$. The unit cell includes three atoms for fcc lattices and two atoms for a hexagonal lattice. [Hexagonal systems are usually described in Bravais–Miller indices ($HKJL$) with the redundant index $J=-H-K$]. Using the cubic lattice constants d_{110} and d_{111}, the size of the fcc unit cell is given by $a_1=a_2=a_0/\sqrt{2}(=d_{110})$, and $a_3=\sqrt{3}\times a_0(=d_{111})$. This choice of unit cell is convenient for surface x-ray diffraction experiments on the (111) surface of cubic crystals since the L direction is now normal to the surface. (Note here that for an ordered $L1_2$ structure, such as for Cu_3Au, a unit cell with twice as large a_1 and a_2 is required) Fig. 12 shows the reciprocal space in the (HL) plane ($K=0$) for close-packed single-element crystals with a (111)-oriented surface. In Fig. 12 (right) side views of the structures are shown [fcc crystal (a), a corresponding fcc twin crystal (b), and hcp crystal (c)]. The sketch of the reciprocal space includes the crystal truncation rods (CTRs) running through the Bragg peaks along the surface normal. These rods are caused by the truncation of the bulk by a (smooth) surface or interface. Those CTRs of the fcc structure, which are not running through in-plane Bragg peaks, are sensitive to the stacking, i.e., the ABC, CBA, and ABA sequences can be distinguished by the location of the Bragg peak positions along these rods. In the hexagonal coordinates (HKL) chosen for the fcc lattice, the L values for Bragg peaks are at $L=1+3n$ or $L=2+3n$ for fcc structures and $L=1.5$ m for hcp structures along these specific CTRs, with integer n,m. The first-order specular Bragg peak is noted as the (003) for the fcc lattice. If we denote the peaks of the hexagonal lattice using the hexagonal unit cell, the c axis of which is 1/3 shorter than the c axis of the hexagonal unit cell for the fcc lattice, the (0002) reflection for the hcp lattices will appear at the same position as the (003) (in hexagonal coordinates) reflection of the fcc lattice if the nearest-neighbor distance (atom size in our hard-ball model) is the same in both crystals.

For the $Cu_3Au(111)$ surface unit cell a_1 and a_2 are two times larger than for a fcc lattice because of the $L1_2$ chemical order. The corresponding reciprocal a_1^* and a_2^* vectors are half of the value for a fcc lattice. The (2, 0) rod in $Cu_3Au(111)$ surface coordinates corresponds therefore to the (1, 0) rod in usual hexagonal coordinates for a fcc system without chemical order. It is sometimes also called "fundamental" rod and contains information on the stacking of the layers only, not on the chemical order within the layers. The above discussion can be directly applied to our measurements of Cu_3Au because we have only investigated CTRs from the fundamental fcc structure of the Cu_3Au crystal (compare to Fig. 3).

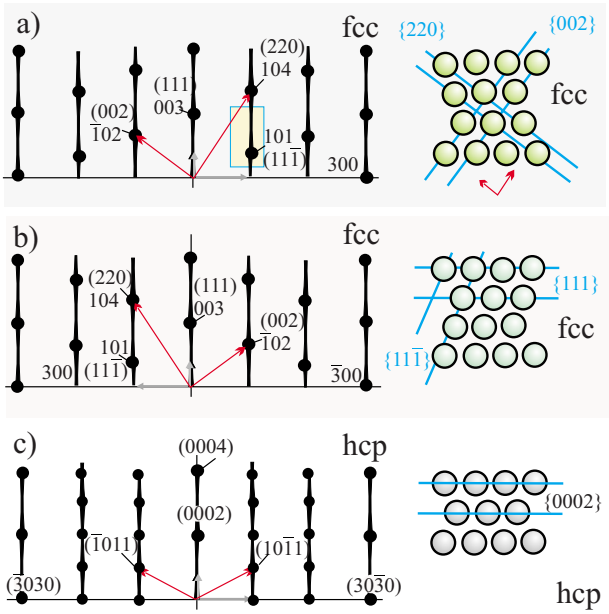

FIG. 12. (Color online) Left hand side: Sketch of the reciprocal space of close-packed crystals indexed in surface coordinates (corresponding to a trigonal unit cell). The usual cubic indices are given in brackets for comparison. Right hand side: Schematic of the crystal surface in real space in cross-sectional view. Some lattice planes are indicated. The fcc crystals in (a) and (b) and the related reciprocal space are equivalent but rotated 180 degree around the [001] axis ([111] axis in bulk notation) relative to each other, which corresponds to an inverted stacking sequence (ABC vs CBA). (c) The case for an hcp crystal (ABA). The rectangular regions indicate the range of the reciprocal space maps in Fig. 4.

*Corresponding author. Present address: Max-Planck-Institut für Eisenforschung, Max-Planck-Straße 1, 40237 Düsseldorf, Germany; f.renner@mpie.de

[1] G. H. Koch, M. P. H. Brongers, N. G. Thompson, Y. P. Virmani, and J. H. Payer, FHWA-RD-01-156, Federal Highway Administration, U.S. Department of Transportation, Washington, D.C., March 2002.
[2] G. Tammann, Z. Anorg. Allg. Chem. **107**, 1 (1919).
[3] L. Graf, Z. Metallkd. **46**, 378 (1955).
[4] H. Gerischer and H. Rickert, Z. Metallkd. **46**, 681 (1955).
[5] L. B. Hunt, Gold Bull. (Geneva) **9**, 24 (1976).
[6] H. Lechtman, Sci. Am. **250**, 38 (1984).
[7] H. Kaiser and G. A. Eckstein, *Encyclopedia of Electrochemistry* (Wiley, Weinheim, 2003), Vol. 4.
[8] H. W. Pickering, Corros. Sci. **23**, 1107 (1983).
[9] E. Schofield, Trans. Inst. Met. Finish. **83**, 35 (2005).
[10] R. Li and K. Sieradzki, Phys. Rev. Lett. **68**, 1168 (1992).
[11] S. Parida, D. Kramer, C. A. Volkert, H. Rosner, J. Erlebacher, and J. Weissmuller, Phys. Rev. Lett. **97**, 035504 (2006).
[12] J. Rugolo, J. Erlebacher, and K. Sieradzki, Nat. Mater. **5**, 946 (2006).
[13] M. Raney, U.S. Patent 1628190 (1927).

[14] Y. Ding, M. W. Chen, and J. Erlebacher, J. Am. Chem. Soc. **126**, 6876 (2004).
[15] D. V. Pugh, A. Dursun, and S. G. Corcoran, J. Mater. Res. **18**, 216 (2003).
[16] A. M. Hodge, J. Biener, L. L. Hsiung, Y. M. Wang, A. V. Hamza, and J. H. Satcher, Jr., J. Mater. Res. **20**, 554 (2005).
[17] D. Kramer, R. N. Viswanath, and J. Weissmueller, Nano Lett. **4**, 793 (2004).
[18] A. J. Forty and G. A. Rowlands, Philos. Mag. A **43**, 171 (1980).
[19] I. C. Oppenheim, D. J. Trevor, Ch. E. D. Chidsey, P. L. Trevor, and K. Sieradzki, Science **254**, 687 (1991).
[20] S. J. Chen, F. Sanz, D. F. Ogletree, V. M. Hallmark, T. M. Devine, and M. Salmeron, Surf. Sci. **292**, 289 (1993).
[21] G. A. Eckstein, Ph.D. thesis, Universität Erlangen, 2001.
[22] M. Stratmann and M. Rohwerder, Nature (London) **410**, 420 (2001).
[23] R. C. Newman, S. G. Corcoran, J. Erlebacher, M. J. Aziz, and K. Sieradzki, Mater. Res. Bull. **24**, 23 (1999).
[24] J. Erlebacher, M. J. Aziz, A. Karma, M. Dimitrov, and K. Sieradzki, Nature (London) **410**, 450 (2001).
[25] J. Erlebacher, J. Electrochem. Soc. **151**, C614 (2004).
[26] F. U. Renner, A. Stierle, H. Dosch, D. M. Kolb, T. L. Lee, and J. Zegenhagen, Nature (London) **439**, 707 (2006).
[27] A. Stierle, A. Steinhauser, A. Rühm, F. U. Renner, R. Weigel, N. Kasper, and H. Dosch, Rev. Sci. Instrum. **75**, 5302 (2004).
[28] G. Materlik, M. Schmäh, J. Zegenhagen, and W. Uelhoff, Ber. Bunsenges. Phys. Chem. **91**, 292 (1987).
[29] M. Fleischman and B. W. Mao, J. Electroanal. Chem. Interfacial Electrochem. **229**, 125 (1987).
[30] M. G. Samant, M. F. Toney, G. L. Borges, L. Blum, and O. R. Melroy, Surf. Sci. **193**, L29 (1988).
[31] Z. Nagy, H. You, R. M. Yonco, C A. Melendres, W. Yun, and V. A. Maroni, Electrochim. Acta **36**, 209 (1991).
[32] B. M. Ocko, J. Wang, A. Davenport, and H. Isaacs, Phys. Rev. Lett. **65**, 1466 (1990).
[33] J. Zegenhagen, A. Kazimirov, G. Scherb, D. M. Kolb, D.-M. Smilgies, and R. Feidenhans'l, Surf. Sci. **352-254**, 346 (1996).
[34] T. Kondo, K. Tamura, M. Takahasi, J. Mizuki, and K. Uosaki, Electrochim. Acta **47**, 2075 (2002).
[35] E. Vlieg, J. Appl. Crystallogr. **30**, 532 (1997).
[36] E. Vlieg, J. Appl. Crystallogr. **33**, 401 (2000).
[37] M. Pourbaix, *Atlas d'Equilibres Electrochemique* (Gauthier-Villars, Paris, 1963).
[38] J. Erlebacher, J. Electrochem. Soc. **151**, C614 (2004).
[39] A. Dursun, D. V. Pugh, and S. G. Corcoran, J. Electrochem. Soc. **152**, B65 (2005).
[40] The lattice plane distance and reciprocal position is 133 pm and (2, 2, 0), respectively, for the Cu_3Au substrate, and 144 pm and (1.84, 1.84, 0) for an epitaxially aligned Au film.
[41] The in-plane rocking width is about 1^0-2^0, in reciprocal space only slightly larger than the radial width. Part of the transversal width is therefore originating, in addition to a small mosaicity of the crystalline layer, from a size broadening.
[42] H. Hong and R. J. Birgeneau, Z. Phys. B: Condens. Matter **77**, 413 (1989).
[43] I. K. Robinson and D. J. Tweet, Rep. Prog. Phys. **55**, 599 (1992).
[44] X. Torrelles, J. Zegenhagen, J. Rius, T. Gloege, L. X. Cao, and W. Moritz, Surf. Sci. **589**, 184 (2005).
[45] M. Aguilar, E. Anguiano, J. A. Aznárez, and J. L. Sacedón, Surf. Sci. **482-485**, 935 (2001).
[46] R. Schuster, D. Thron, M. Binetti, X. Xia, and G. Ertl, Phys. Rev. Lett. **91**, 066101 (2003).
[47] J. Jacobsen, L. P. Nielsen, F. Besenbacher, I. Stensgaard, E. Laegsgaard, T. Rasmussen, K. W. Jacobsen, and J. K. Nørskov, Phys. Rev. Lett. **75**, 489 (1995).
[48] T. E. Jones, T. C. Q. Noakes, P. Bailey, and C. J. Baddeley, Surf. Sci. **600**, 2129 (2006).
[49] K. Umezawa, S. Nakanishi, and W. M. Gibson, Phys. Rev. B **57**, 8842 (1998).
[50] K. Umezawa, T. Ito, S. Nakanishi, and W. M. Gibson, Appl. Surf. Sci.s fo **219**, 102 (2003).
[51] O. M. Magnussen, J. Scherer, B. M. Ocko, and R. J. Behm, J. Phys. Chem. B **104**, 1222 (2000).
[52] Y. Chu, I. K. Robinson, and A. A. Gewirth, J. Chem. Phys. **110**, 5952 (1999).
[53] R. T. Tung, J. M. Gibson, and J. M. Poate, Phys. Rev. Lett. **50**, 429 (1983).
[54] H. Fujitani, Phys. Rev. B **57**, 8801 (1998).
[55] H. W. Pickering and C. Wagner, J. Electrochem. Soc. **114**, 698 (1967).
[56] F. U. Renner, A. Stierle, H. Dosch, D. M. Kolb, and J. Zegenhagen, Electrochem. Commun. **9**, 1639 (2007).
[57] D. Wolf, Appl. Phys. Lett. **58**, 2081 (1991).
[58] Z. Shi, S. Wu, and J. Lipkowski, Electrochim. Acta **40**, 9 (1995), and references herein.
[59] T. P. Moffat, F.-R. F. Fan, and A. J. Bard, J. Electrochem. Soc. **138**, 3224 (1991).